ChemCatChem

Research Article
doi.org/10.1002/cctc.202200240

Chemistry Europe
European Chemical Societies Publishing

www.chemcatchem.org

Special Issue

Dynamics of Reaction-Induced Changes of Model-Type Iron Oxide Phases in the CO_2-Fischer-Tropsch-Synthesis

Aleks Arinchtein,[a] Meng-Yang Ye,[a] Qingxin Yang,[b] Carsten Kreyenschulte,[b] Andreas Wagner,[c] Marvin Frisch,[a] Angelika Brückner,[b] Evgenii Kondratenko,[b] and Ralph Kraehnert*[a]

Iron-based catalysts are employed in CO_2-FTS due to their ability to convert CO_2 into CO in a first step and their selectivity towards higher hydrocarbons in a second CO hydrogenation step. According to the literature, iron carbides represent the active phase for hydrocarbon formation and are claimed to emerge in the presence of CO. We propose nanostructured FeO_x films as model systems to assess information about the complex phase transformations during CO_2-FTS. Mesoporous hematite, ferrihydrite, maghemite, maghemite/magnetite films were exposed to CO_2-FTS atmospheres at 20 bar and 300 °C. Up to three distinct phases were observed depending on the time-on-stream (TOS): a sintered maghemite/magnetite phase, a carbidic core-shell structure, and a low-crystalline, needle-type oxide phase. Our findings indicate that the formation of an intermediary maghemite/magnetite phase, predominant after short TOS (30 h), precedes the evolution of the carbide phase. Yet, even after prolonged TOS (185 h), no full conversion into a bulk carbide is observed.

Introduction

The catalytic reduction of CO_2 *via* hydrogenation is a highly promising concept to recycle large amounts of exhausted CO_2 gas in the chemical industry, generating value-added or platform chemicals.[1,2] The hydrogenation of CO_2 into higher hydrocarbons can be performed on iron- or cobalt-based catalysts in the CO_2-Fischer-Tropsch synthesis (CO_2-FTS). On the basis of CO_2-FTS, kerosene and other synthetic fuels can be produced using green hydrogen from renewable energy sources.

According to the literature,[3–5] the first step of CO_2-FTS relies on the conversion of CO_2 into CO *via* the reverse water-gas shift (RWGS) reaction. Subsequently, the formed CO is converted into hydrocarbons *via* typical CO-Fischer-Tropsch synthesis (CO-FTS). Iron-based catalysts are the most promising candidates, due to their ability to catalyze both the RWGS as well as the CO-FTS reactions under similar reaction conditions with high selectivity toward higher hydrocarbons.[6,7]

In CO_2-FTS, temperature and partial pressure of the reactants appear to be critical, as they affect reaction kinetics and surface states. Iron-based catalysts were reported to undergo complex morphological and structural changes manifested in the formation of various oxide and carbide phases.[7] For instance, hematite (α-Fe_2O_3) was reported to form wustite (FeO), maghemite (γ-Fe_2O_3), elemental iron (Fe), cementite (θ-Fe_3C) and Hägg iron (χ-Fe_5C_2) under the conditions of CO_2-FTS. The emerging phases show a strong impact on catalyst activity and selectivity.[7–11] Thus, the reaction-induced phase transformations and the different surface reactivity result in a highly complex, dynamic behavior. Beyond that, metal-support interactions can alter the catalytic properties.[12] Moreover, the promotion with e.g. alkali metal ions was reported to increase catalytic activity.[13–15]

Understanding the complex interplay between different phases requires a decoupling of the relevant parameters, such as initial phase vs. reaction conditions and time of exposure to different reactants. In a previous work, we reported the synthesis of different structurally defined iron oxide phases as model systems to unravel phase transformation mechanisms and kinetics.[16] The mesoporous iron oxide films can be synthesized with different initial phase composition, *i.e.* hematite,[16] ferrihydrite,[16] maghemite,[17] as well as a maghemite partially converted into magnetite.[17] We previously employed this approach to investigate phase transformation and crystallization behavior of iron oxides and/or -oxohydr-

[a] *A. Arinchtein, M.-Y. Ye, M. Frisch, Dr. R. Kraehnert*
Department of Chemistry
Technische Universität Berlin
Strasse des 17. Juni 124
D-10623, Berlin (Germany)
E-mail: ralph.kraehnert@tu-berlin.de
[b] *Q. Yang, Dr. C. Kreyenschulte, Prof. A. Brückner, Prof. E. Kondratenko*
Leibniz-Institut für Katalyse e.V
Albert-Einstein-Str. 29a
D-18059, Rostock (Germany)
[c] *A. Wagner*
Division 6.1 Surface Chemistry and Interface Analysis
Federal Institute for Materials Research and Testing (BAM)
Unter den Eichen 44–46
D-12203 Berlin (Germany)

Supporting information for this article is available on the WWW under https://doi.org/10.1002/cctc.202200240

This publication is part of a joint Special Collection with ChemElectroChem on "Catalysts and Reactors under Dynamic Conditions for Energy Storage and Conversion (DynaKat)". Please check our href="https://chemistry-europe.onlinelibrary.wiley.com/doi/toc/10.1002/(ISSN)1867-3899.DynaKat"homepage for more articles in the collection.

oxides upon exposure to air,[16] N_2,[17] Ar/H_2[17] as well as the role of water[18] in oxide phase transformations. These films have well defined properties i.e. crystallite and pore sizes as well as phase composition. Local changes observed in e.g. SEM can be applied to the whole films. Moreover, the pore structure act as an indicator for changes in the morphology. Since CO was reported to be an important reaction intermediate, we recently studied the effects of different FeO_x phases exposed to mixtures of CO/H_2 using electron microscopy and diffraction techniques in order to connect phase transformations on different length scales. Independent of the initial iron oxide phase (hematite "HEM", ferrihydrite "FH", maghemite "MAGH", maghemite/magnetite "MAGH/MAGN"), a complete transformation into iron carbides was observed upon CO/H_2 exposure at 300 °C and atmospheric pressure within less than 20 h time-on-stream (TOS). Importantly, the formed carbides mostly retained their templated mesopore structure.

The present study increases the complexity of the catalyst treatment toward CO_2-FTS conditions, *i.e.* mixtures of CO_2 and H_2 at high pressures (20 bar) and varying exposure time (30 and 185 h). Comprehensive physicochemical characterization methods (SEM, TEM, STEM-EELS, SAM, SAED, XPS) were used to assess the dynamics of local and surface/bulk averaged phase transformations for HEM, FH, MAGH and MAGH/MAGN oxide films.

The combined analysis reveals a dynamic material behavior of significantly higher complexity compared to CO/H_2 treatments.[19] The formation of predominantly oxidic domains can be already observed to some extent after 30 h TOS. After 185 h, up to three distinct phases are formed: a weakly sintered, a strongly sintered and a needle-like phase. The phases are arranged in domains of varying average sizes and morphological features, depending on the initial iron oxide phase and TOS. Mechanistic, kinetic and practical implications of the observed complex behavior are discussed.

Approach

Scheme 1 outlines the approach of the present study. Iron oxide films with templated pore structure and different phase composition were prepared *via* the EISA (evaporation induced self assembly) approach, adapting synthesis routes from previous works.[16–19] Briefly, this sol-gel process employs soft templates e.g. block-copolymer for the synthesis of well-defined mesoporous films. It relies on fast evaporation of solvents, formation of a metal-polymer hybrid mesophase and condensation of e.g. metal precursor around the soft template.[20,21] These films were exposed to CO_2/H_2 feeds at 20 bar and 300 °C for different TOS (30 and 185 h) with a gas flow of 3.8 mL/min.

Ex-situ analysis of the obtained materials was performed to assess the reaction-induced structural and morphological changes using scanning electron microscopy (SEM) and transmission electron microscopy (TEM). The phase composition was *investigated* by selected area electron diffraction (SAED). Surface composition was studied *via* X-ray photoelectron spectroscopy (XPS). Scanning Auger Microscopy (SAM) was used to connect local Auger spectra with microscopy-derived morphologies. Scanning transmission electron microscopy coupled with electron energy loss spectroscopy (STEM-EELS) was employed for high-resolution local phase analysis

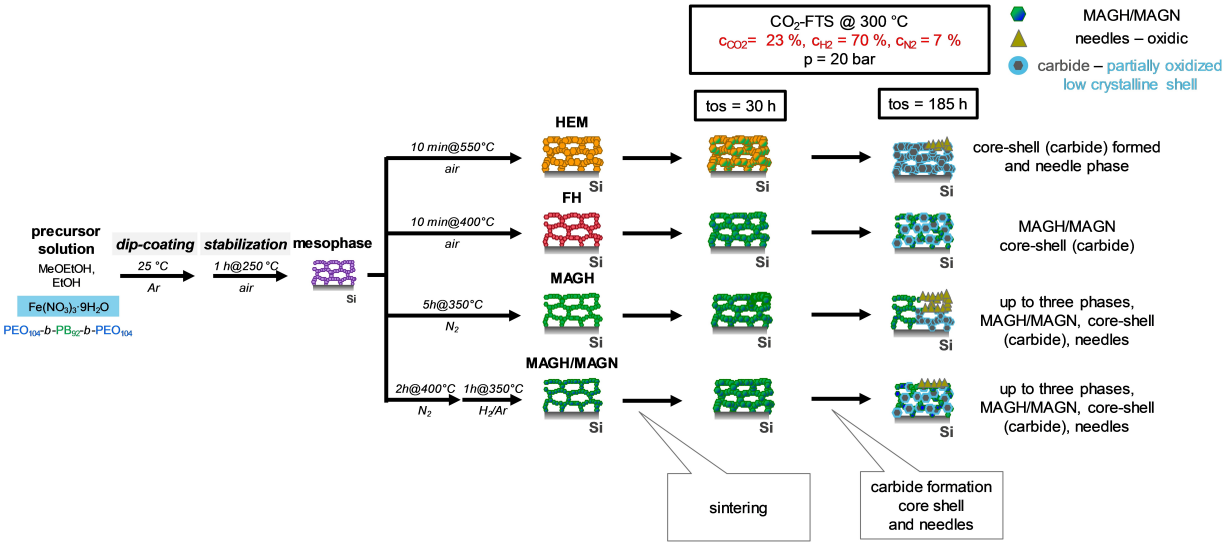

Scheme 1. Approach for the synthesis of mesoporous iron oxide films with different initial phase composition and subsequent treatment under realistic conditions of the CO_2-FTS reaction for 30 and 185 h TOS. Dip-coating of flat silicon substrates and calcination at 250 °C in air for 1 h yields the mesophase which is further treated in different atmospheres to obtain HEM (air), FH (air), MAGH (N_2) and MAGH/MAGN (N_2, then H_2/Ar). Exposure to CO_2-FTS conditions induces controlled phase transformations. After 30 h TOS, sintering of the samples can be observed and the formation of domains with a second phase for FH and MAGH. Up to three phases can be observed after 185 h: a strongly sintered phase, core-shell structures with a crystalline carbide core and a partially oxidized, low-crystalline oxide shell, as well as domains with needles.

Results and Discussion

The most important structural features of the synthesized HEM, FH, MAGH and MAGH/MAGN oxides films are summarized in Figure S1. The results are well in-line with our previous findings.[18,19] Due to their homogeneous structure, these oxide films featuring varying composition, crystallinity and average oxidation states of the iron species are ideal starting systems for an evaluation of reaction-induced changes during CO_2-FTS.

30 h TOS under CO_2-FTS conditions

Figure 1 displays SEM (I, II, III) and TEM (IV, V) images along with SAED analysis (VI) recorded for all spent oxide materials after CO_2/H_2-treatments at 300 °C for 30 h TOS. In order to assess the different length scales of phase transformation, representative electron microscopy images are provided at varying magnifications. Different morphological features observed in low magnification (I), *i.e.* different domains of emerging phases, were further investigated at higher resolution (e.g. b-II–B, c-II). The drawings given on the right side of the figure schematically illustrate the derived understandings of the respective local structures and phase compositions for each oxide model system.

The crystallites of HEM films were strongly sintered after 30 h TOS, as evidenced by top-view SEM imaging (Figure 1a-I/II/III). Lattice fringes visible in the TEM images of 0.48 and 0.25 nm can be assigned to a mixture of MAGH/MAGN (Figure 1a-V). Similar to fresh HEM films, the SAED pattern features only a few diffraction spots typical for highly crystalline materials, and can be assigned to MAGH/MAGN alongside a residual HEM phase.

Spent FH films undergo significant sintering of the crystallites resulting in mesopores with a reduced degree of local order (Figure 1b-II–A). Moreover, the formation of distinct domains with a second phase with larger crystallites of brighter contrast can be resolved (Figure 1b-II–B). Corresponding lattice fringes of 0.48 nm and 0.30 nm were found (Figure 1b-V), which represent characteristic values for MAGH and/or MAGN which is further validated by the recorded SAED pattern (Figure 1b-VI). For the second phase, it was not possible to collect any phase information due to the limited amount in the film. Probably, this second phase with minor contribution represents a carbide phase, but it is also possible that other phases such as wustite or elemental iron were formed due to the reductive atmosphere.

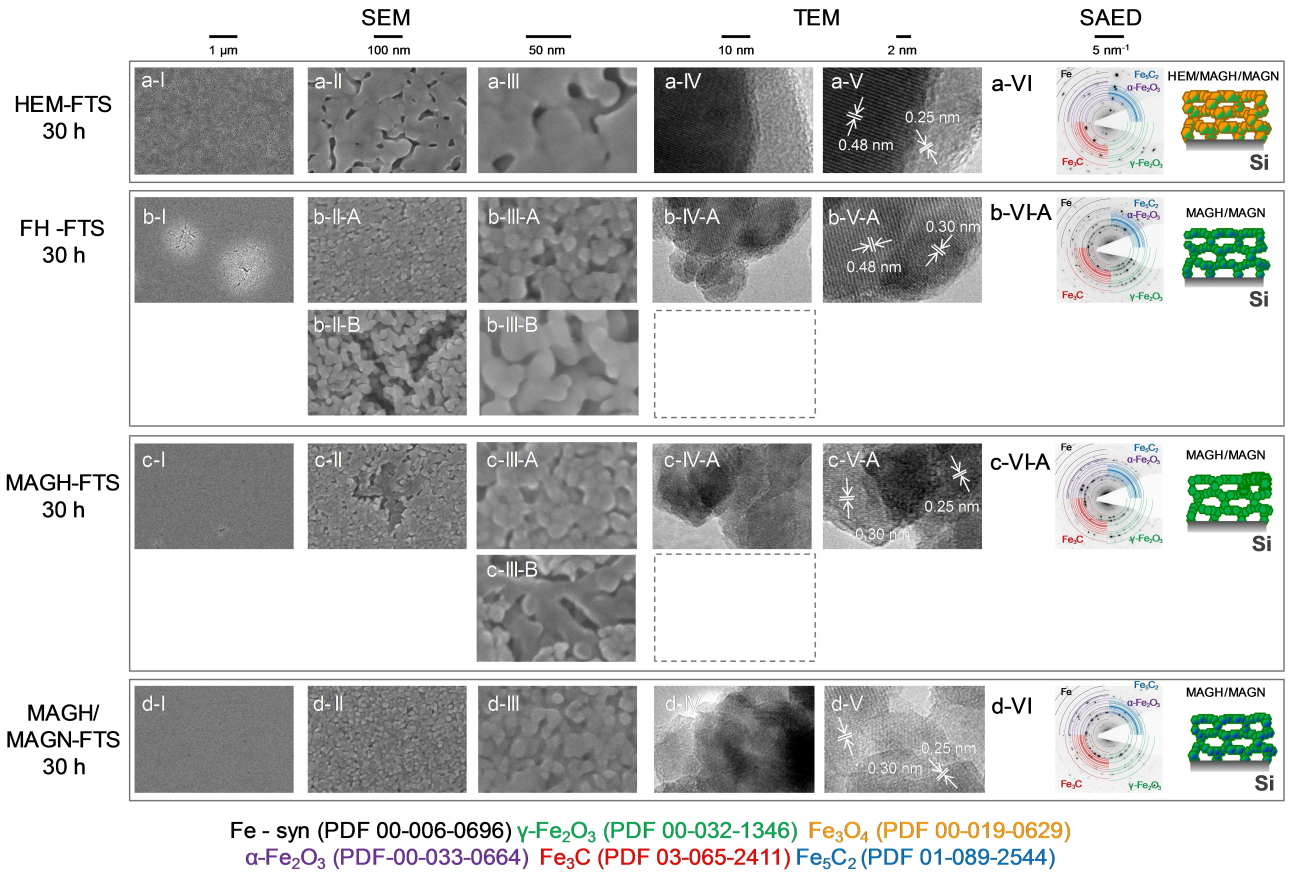

Figure 1. Iron oxide films treated in conditions of the CO_2-FTS at 300 °C, 20 bar for 30 h in to $H_2/CO_2/N_2 = 3:1:0.3$. Following iron oxides have been employed: (a) HEM, (b) FH, (c) MAGH, (d) MAGH/MAGN. All samples were characterized by top-view SEM (I/II/III), TEM (IV/V) and SAED (VI). Domain formation was observed for FH (b-III–B) and MAGH (c-III–B). Higher magnification SEM images show representative areas of each sample.

Spent MAGH films reveal similar structural features as spent FH materials after 30 h TOS, showing a sintered mesoporous structure, as illustrated in top-view SEM images (Figure 1c-I/II/III). Two morphologies can be differentiated, sintered mesopores (Figure 1 c-III–A) as the main phase which contain small domains with larger sintered morphology as a second phase (Figure 1c-III–B). Lattice fringes of 0.30 and 0.25 nm (see TEM images in Figure 1 c-V) match well with MAGH/MAGN and are consistent with the SAED pattern (Figure 1c-VI).

Spent MAGH/MAGN films undergo similar sintering effects as spent FH and MAGH oxides (Figure 1d-I/II/III). However, homogeneous, domain-free films were obtained, in which MAGH/MAGN is indicated to represent the main phase according to TEM (Figure 1d-V) and SAED (Figure 1d-VI) analyses, and no indication for any carbide formation can be found.

In brief, spent FH and MAGH films formed domains with a second phase that likely represents an intermediate phase in the carbide formation pathway. Moreover, oxides synthesized *via* thermal treatment in an inert or reducing atmosphere prior to the H_2/CO_2 treatment show a higher resistance to pronounced sintering compared to films calcined in air.

185 h TOS under CO_2-FTS conditions

Aiming at a more profound understanding of the dynamic behavior of iron-based oxides under CO_2-FTS conditions, the same characterization methods except for GI-XRD were applied after an extended TOS of 185 h (see Figure 2). Due to the limited sample amount, GI-XRD analysis was not applicable. Compared to the results after 30 h TOS (Figure 1) discussed above, more pronounced structural changes are visible for all investigated oxide materials. Careful phase analysis reveals the complex reaction-induced transformations, leading to the evolution of iron carbide phases in coexistence with oxidic domains.

In HEM, the prolonged TOS for H_2/CO_2 treatment induces the formation of two distinct phases, as revealed by top-view SEM (Figure 2a-I), *i.e.* a strongly sintered phase (Figure 2a-II/III–A) alongside a needle-type phase with darker electron contrast (Figure 2a-II/III–B). The latter can be found in rather low amounts and features a worm-like structure (SI 3). Besides, TEM images reveal a core-shell structure for the sintered phase (Figure 2a-IV/V), which is likely to represent a carbide phase, as the diffraction spots in the SAED can be well aligned with Fe_5C_2 (Figure 3a-VI). It has been shown in our previous work that mesoporous iron carbide films exhibit a core shell structure with a crystalline carbide core and a partially oxidized carbide shell.[19]

Spent FH films reveal pronounced crystallite growth without any observable domain formation or macroscopic segregation (Figure 2b-I/II/III). TEM analysis indicates the presence of two distinct phases with lattice fringes of 0.29 nm (Figure 2b-IV/V–A), observable in MAGH/MAGN, alongside a core-shell phase (Figure 2b-IV/V–B). Results from comprehensive SAED analysis suggest a mixed MAGH/MAGN phase to prevail (Figure 2b-VI) with minor contributions of a carbide phase, in good agreement with the observed core-shell structures.

Spent MAGH films show a more complex topology with some features already being found in the spent HEM and FH films. For MAGH films, however, three distinct phases emerge (Figure 2c-I) that can be distinguished by variations in electron contrast in top-view SEM and, beyond that, by differences in morphology. First, a comparably minor amount of a strongly sintered phase, similar to that observed in spent HEM films (Figure 2c-II/III–A), is found. Second, a morphology composed of smaller crystallites appearing to be fused together (Figure 2c-II/III–B) can be observed. Third, a needle-like phase is found, similar to the one present in spent HEM films (Figure 2c-II/III–C). SAED analysis was used as a next step to identify correlations of the observed morphologies with distinct phases. The diffraction pattern from core-shell structures evident from TEM images of the strongly sintered phase (Figure 2c-IV/V–A) corresponds well to Fe_5C_2 (Figure 2c-VI–A). Concerning the sintered smaller crystallites, lattice fringes of 0.48 nm (Figure 2c-IV/V–B) and the SAED pattern (Figure 2c-VI–B) can be assigned to either MAGH, MAGN or a mixture of them, *i.e.* MAGH/MAGN. Note that a clear assignment to any of these phases is not possible from our data due to the structural similarity of both phases. The third phase appears to be a low-crystalline material (Figure 2c-IV/V–C) with few spots forming rings in the SAED pattern which correspond to MAGH/MAGN (Figure 2c-V–C). Results from Scanning Auger Microscopy (SAM) clearly suggest that all phases contain iron, oxygen and carbon. Due to the high surface-sensitivity of the method, an iron oxide phase seems to be present at the catalyst surface for all three phases. Hence, we assume that the needle-type phase is a low-crystalline iron oxide phase. Moreover, the described three phases were all observed in TEM and comprehensive SAED analysis confirms their respective phase (SI 4).

For spent MAGH/MAGN films, again, three different phases are found (Figure 2d-I). Higher magnifications (Figure 2d-II–A) show that the strongly sintered phase (Figure 2d-III–A) is evenly mixed with the less sintered one (Figure 2d-III–B), while a needle-like morphology has been identified as a third phase (Figure 2d-III–C). TEM analysis reveals a core-shell structure for the strongly sintered phase (Figure 2d-IV/V–A). Lattice fringes of 0.22 nm correspond to the (202) lattice planes of Fe_5C_2, which is further corroborated by the respective SAED-pattern (Figure 2d-VI–A/B). Similar to spent FH as well as MAGH films, the sintered smaller crystallites represent a MAGH/MAGH phase, as indicated by the appearance of lattice fringes of 0.30 and 0.25 nm spacing (Figure 2d-IV/V–B) and the SAED pattern (Figure 2d-VI–A/B).

In brief, our findings suggest an influence of the pretreatment (*i.e.* phase) of the iron oxide starting material on the degree of crystallite growth after 30 h TOS under CO_2-FTS conditions. Partially pre-reduced starting materials (MAGH/MAGN) show a higher morphological stability, *i.e.* an improved sintering resistance, compared to more oxidized iron oxides (HEM).

A prolonged TOS, *i.e.* 185 h, leads to the development of complex structural and morphological features. Importantly, the formation of iron carbides proceeds from reduced iron oxides,

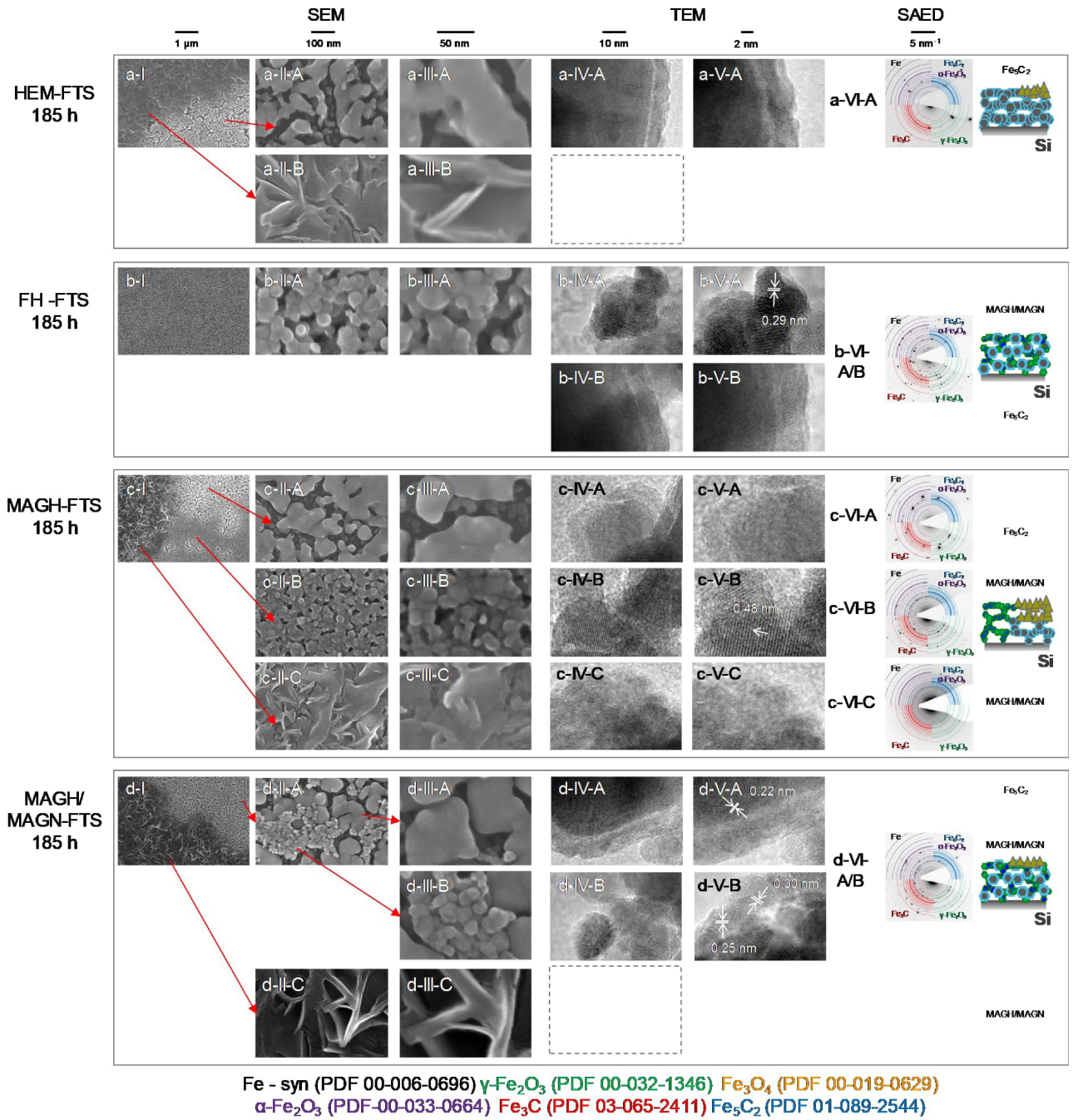

Figure 2. Iron oxide samples after CO_2-FTS treatment at 300 °C, 20 bar for 185 h. (a) HEM, (b) FH, (c) MAGH and (d) MAGH/MAGN. All samples were characterized by top-view SEM (I/II/III), TEM (IV/V) and SAED (VI). Up to three phases were resolved and annotated as xx-xx-A, -B or -C, respectively. Higher magnification SEM images show representative areas of each sample.

i.e. MAGH/MAGN, that are the predominant phases after short TOS (30 h) for all model systems. After 185 h, a sintered carbide phase develops for all films except for FH. We thus conclude that FH shows the lowest tendency for iron carbide formation and, concomitantly, excessive crystallite growth. MAGH and MAGH/MAGN oxides were converted into films with well-distributed carbide and oxidic MAGH/MAGN phases that are strongly sintered or less sintered, respectively. Compared to the syngas treatment described in our previous work,[19] more complex structures are observed in this study.

Domains with predominantly oxidic and carbidic phase coexist, even after 185 h TOS. For MAGH films, small domains can already be observed after short TOS, which are likely to serve as nucleation spots for the carbide formation. Even if MAGH/MAGN films show a rather homogeneous morphology and porosity after short TOS, a highly complex structure with three different morphologies results after prolonged TOS.

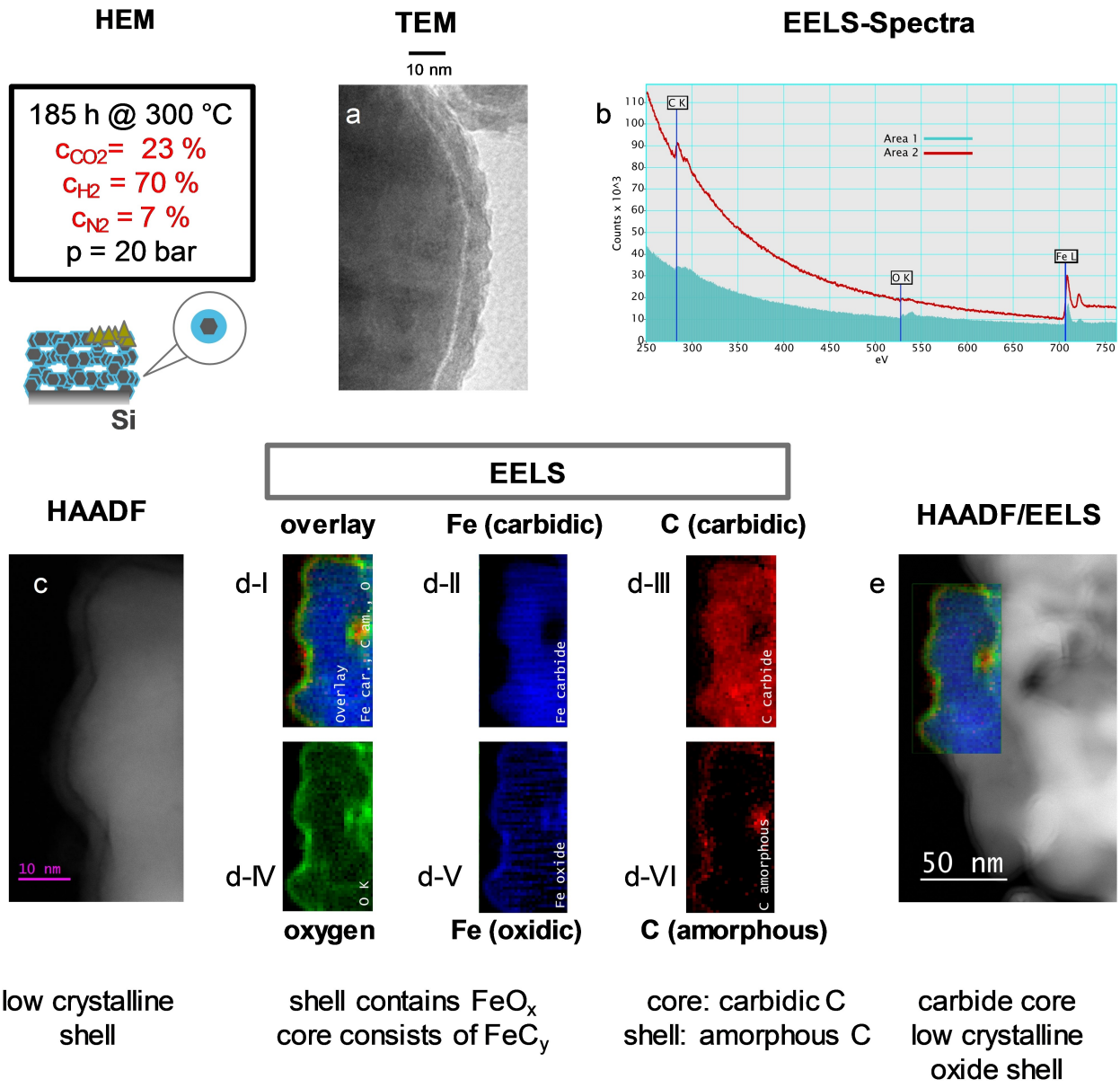

Figure 3. HEM film after CO_2-FTS treatment at 300 °C, 20 bar for 185 h analyzed by STEM-EELS. a) TEM image where the core/shell structure has been observed. b) STEM-EELS spectra to distinguish the elements. c) HAADF of the core/shell structure. d) STEM-EELS mapping divided into overlay (I), carbidic Fe (II), carbidic C (III), O (IV), oxidic Fe (V) and amorphous C (VI). e) Overlay of combined EELS signals and HAADF.

Phase analysis via STEM-EELS

HEM films treated for 185 h were exemplarily analyzed *via* STEM-EELS (Figure 3) to determine the phase composition of the core-shell structure observed in TEM microscopy (Figure 2a-IV–A). HAADF images (Figure SI 5) confirmed the low-crystalline character of the thin shell. Figure 3 provides representative results for spent HEM films after 185 h TOS. A shell thickness of 4–5 nm (Figure 3a) is indicated from high-resolution TEM imaging. EELS (Figure 3b) allows to distinguish signals from carbidic or oxidic iron as well as from amorphous carbon by evaluating the differences in fine structures (Figure SI 6).[22] The EELS elemental mappings (Figure 3d) and the derived overlay image (Figure 3e) confirm the presence of an iron carbide phase in the core with an oxidic, low-crystalline shell containing or being surrounded by an amorphous carbon phase. Note that carbon contamination, as a result of hydrocarbon cracking by the electron beam at the surface, might somewhat hinder a clear distinction of carbon species. Nevertheless, the high resolution HAADF-STEM image in Figure 3c illustrates the weakly crystalline character of the shell within the observed core-shell structures.

STEM-EELS analysis was additionally carried out for HEM films treated in syngas atmosphere as a reference based on a procedure reported in our previous work[19] (see SI 7). The EELS mapping provides further evidence for the claimed core-shell

structure and, similar to the CO_2-FTS conditions, amorphous carbon can be detected in the shell. This indicates a similar mechanism for the carbide formation in the previously investigated syngas and the current CO_2-FTS treatment, yet with significant differences in reaction kinetics.

Surface composition analysis via XPS

HEM-based films in fresh as well as CO2-FTS treated state after 30 h and after 185 h TOS were analyzed *via* XPS. Figure 4a displays the respective Fe2p (a-I), O1s (b-I) and C1s (c-I) spectra. Fresh HEM films exhibit a typical spectrum for α-Fe_2O_3 with a major contribution of the multiplet centered at 710.9 eV stemming from Fe (III)[23,24] (Figure 4a-I). Spectra recorded for HEM after 30 h and 185 h TOS present broad and asymmetric doublet peaks centered at 710.6 eV with weak satellites at 716.1 eV that can be typically found in Fe 2p spectra of wustite (FeO).[23] This indicates the partial reduction of Fe(III) species present in the fresh samples during CO_2-FTS conditions. As evidenced by results from STEM-EELS analysis (Figure 3), no iron carbide signals (typically located at 707.9 eV) were observed, highlighting the iron oxide shell with low crystallinity formed after exposure of the materials to air.

The changes can be also tracked in the O 1s XPS spectra for the HEM samples (Figure 4b-I) with increasing TOS. Fresh HEM films show a major contribution for Fe–O at 529.6 eV in the O 1s spectrum,[24] while the two smaller peaks could be ascribed to C=O and C–O originating from adventitious carbon due to adsorbed carbon species after air exposure.[25] After 30 h treatment, Fe–O is still the dominant species in the O 1s spectrum. Yet, after 185 h TOS, this contribution drops significantly in intensity, while the C–O from the adsorbed hydrocarbons becomes the predominant species. Additionally, the surface element composition detected by XPS (Figure 4a-I/c-I) shows that the atomic ratio of Fe:C on the surface dropped from 10:3 (fresh HEM) to 5:3 (HEM after 30 h TOS) and finally to 1:12 (after 185 h TOS), suggesting that the surface of the HEM samples was gradually covered by a rather dense carbon layer. This is in good consistency with the amorphous carbon shell observed for the 185 h treated HEM sample. Carbon deposits on the catalyst surface are possibly formed through the Boudouard reaction and likely account for one possible deactivation process of CO_2-FTS catalysts.[26]

In order to compare the influence of the initially present iron oxide phase respective CO_2-FTS treated films after 30 h TOS were analyzed via XPS. Figure 4b displays the respective Fe2p (a-II), O1s (b-II) and C1s (c-II) spectra. A comparable trend can be observed independent of the phase of the fresh iron oxide.

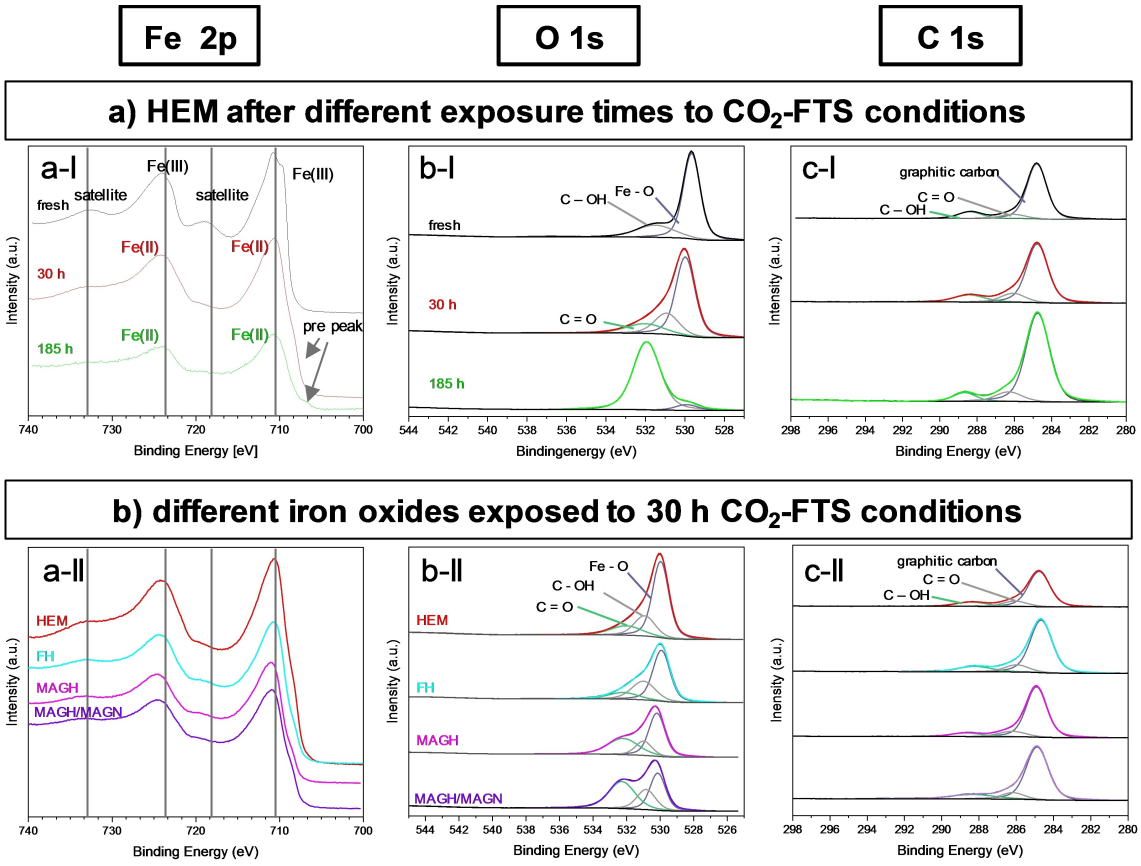

Figure 4. XPS spectra for HEM films after different TOS (fresh, 30 h, 185 h): Fe 2p (a-I), O 1s (b-I), C 1s (c-I). In addition, films treated for 30 h in the CO_2-FTS with different initial phase composition (HEM, FH, MAGH, MAGH/MAGN) were analyzed and the Fe 2p (a-II), O 1s (b-II) as well as C 1s (c-II) spectra are shown.

MAGH, FH, MAGN films after 30 h TOS reveal similar Fe 2p spectra as HEM (Figure 4a-II). FeO can be claimed to be the prevailing species. In case of the O 1s spectra for all materials, the main contribution stems from Fe–O. However, a trend can be observed for C=O and C–O contributions from adsorbed hydrocarbons. Depending on the initial phase composition with lower "oxidation degree", the signal around 532.3 eV increases in intensity in the order HEM < FH < MAGH < MAGH/MAGN, thus indicating a higher carbon coverage for reduced samples. For all C 1s spectra, the main contributions result from C–C/C–H species, while the smaller peak in all spectra can be assigned to C–O/C=O from adsorbed hydrocarbons as observed in previous work.[19] Based on the XPS results, we suggest that in all materials the formed iron carbide phase is densely covered by a thick shell of oxide and/or amorphous carbon and, thus, no contribution of surface carbide species becomes visible in the spectra of the H_2/CO_2-treated materials.

Correlation of phase and morphology via SAM analysis

Scanning Auger Microscopy (SAM)[27] is a powerful technique to examine local changes at the surface of a material at the nanoscale. The depth information of ~5 nm and a lateral resolution of about 5–10 nm render the method an excellent nano-probe for phase analysis. As representative example, we investigated spent MAGH films after 185 h TOS in CO_2-FTS due to the observed complex structural and morphological features.

Each point was measured five times for ten cycles (Figure 5I) and for the line scan 256 points were measured in total (Figure 5III). Point measurements for all three phases showed similar features in the recorded Auger spectra. Iron (~703) eV and oxygen (~510 eV) signals[28] were detected for all three phases, indicating iron oxides on the surface (Figure 5II). Carbon (~275 eV)[29] is also present in all structures. Position 2, which can be assigned to the carbide phase, shows the highest carbon content. Silicon (~88 eV) signals originate from the silicon substrate. A line scan throughout the treated MAGH sample (Figure 5III) confirms the presence of iron and oxygen, underlining the dominating oxide phase at the surface. Moreover,

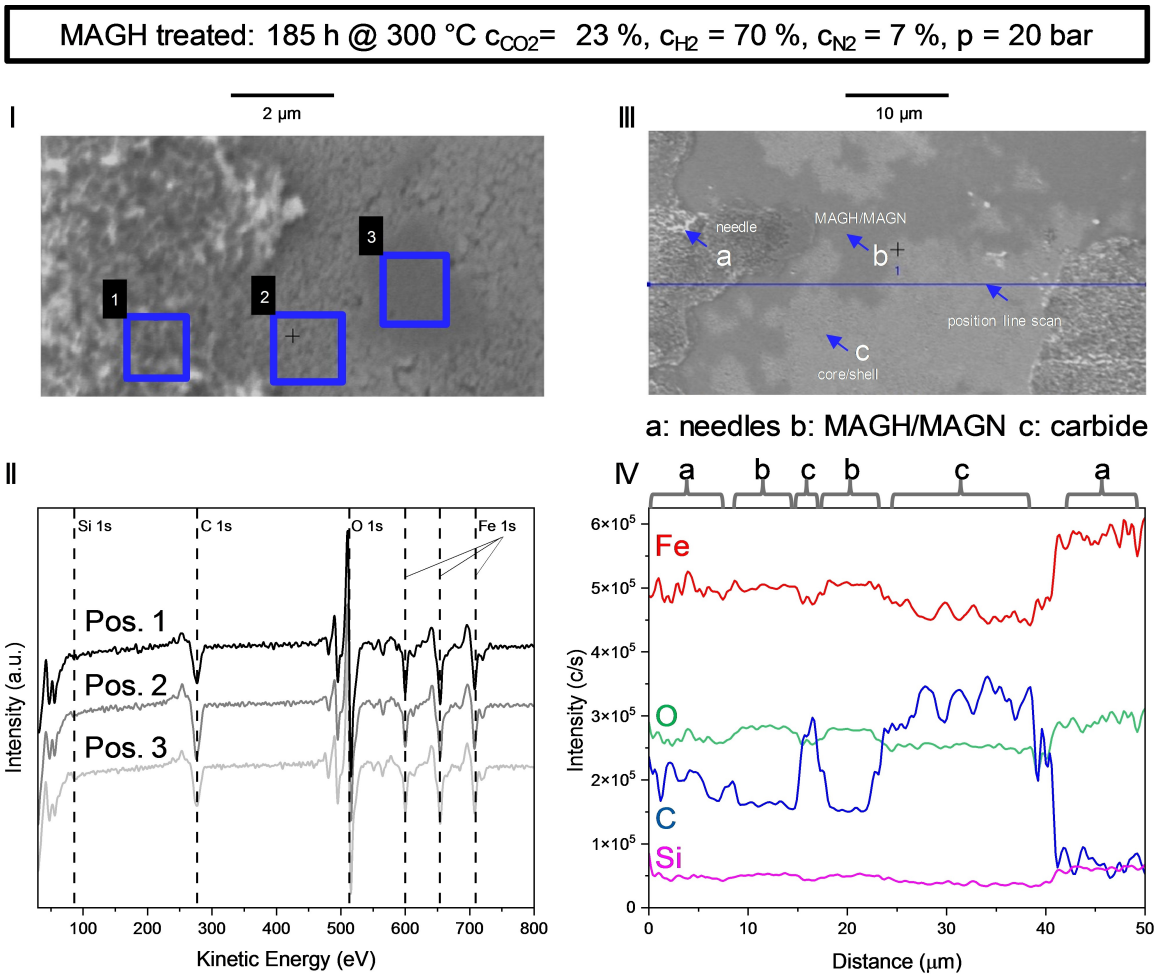

Figure 5. Scanning Auger Microscopy (SAM) Spectroscopy for MAGH treated for 185 h at 20 bar, 300 °C in the CO_2-FTS. I) Representative top-view SEM image for the different scanning AES positions. II) AES spectra for all three positions. III) Top-view SEM image showing the position for the performed scanning AES line-scan (blue line) over all three phases observed in the treated MAGH sample. IV) Elemental AES line-scan over the range of 50 µm shown in III).

pronounced differences in the carbon content were nicely resolved in the spectra (Figure 5IV), suggesting the presence of amorphous carbon in the shell for the carbide phase.

Discussion

The time-on-stream under CO_2-FTS conditions plays a decisive role in the evolution of the distinct structural features observed in all four herein studied iron-based oxides. After short TOS (30 h), a MAGH/MAGN phase seems to prevail. FH and MAGH films begin to form a second phase to small extents. Thereby, local domains with a second sintered phase, potentially representing a wustite or elemental iron phase,[30] emerge. A prolonged TOS of 185 h under CO_2-FTS conditions leads to the formation of up to three phases. A carbide (core-shell) phase can be observed independent of the phase of the initial oxide. For MAGH and MAGH/MAGN films, a weakly sintered MAGH/MAGN phase remained essentially preserved. Except for spent FH, all films contained needle-type structures located inside the carbide domains.

Under the reducing conditions of the CO_2-FTS, iron species in the oxide phases are partially reduced to Fe(II) or even Fe(0). After 30 h TOS, a MAGH/MAGN phase is predominant, independent of the starting material phase. STEM-EELS and scanning AES revealed a high carbon content in HEM treated for 185 h and showed similar features to HEM treated in syngas (SI 7), indicating a similar formation mechanism for both treatments. Moreover, low magnifications for H_2/CO_2-treated MAGH films (SI 3) reveal domains of the carbide phase, which resemble the domains observed for the FH-to-HEM transformation described in our previous work,[16] thus indicating a similar growth mechanism.

Interestingly, the transformation of iron oxides into iron carbides takes more time in CO_2 than in syngas atmosphere at 300 °C, as an entire conversion into a bulk carbide phase is not observed in the present study. In syngas atmospheres, however, bulk carbide formation was found after only 20 h. Here, the initial oxide phase and average metal oxidation state have a great impact on the number and quantity of the formed phases. In this context, complex structural features are observed. Hence, we conclude that an insufficient CO partial pressure for an entire bulk conversion into the corresponding carbide phase was reached over the investigated period of time in the present study. A high CO formation rate was previously reported to promote carbide formation.[31] Similarly, the use of ternary H_2/CO_2/CO feeds is thus expected to increase the carbide fraction in the materials.

In addition, water generated by the reverse water-gas shift reaction (RWGS) is most likely responsible for the re-oxidation of the emerging carbide phase. In CO_2-FTS, the reaction mechanism leads to an increased formation of by-product water compared to classical CO-FTS,[32] which was reported to deactivate active Fe sites in the catalysts. In fact, CO_2 is also known to be able to oxidize iron carbides.[26] Such oxidation processes are generally believed to result in lower activity and selectivity toward heavier hydrocarbons due to a reduced amount of active Hägg iron carbide phase.[32] Riedel *et al.*[31] tracked phase changes of iron-based catalysts in the CO_2-FTS through operando Mössbauer spectroscopy. The authors claimed the formation of an unknown iron oxide phase at about 50 h TOS in the reactor, which was active for the RWGS. Zhang *et al.*[26] investigated Fe_5C_2 catalysts at 330 °C at elevated pressure and were able to resolve a Fe_3O_4 phase using operando Raman spectroscopy. The catalysts were effectively regenerated by oxidation in CO_2 followed by a carburization step in CO to obtain a pure Fe_5C_2 catalyst. Concurrent changes in morphology of the catalysts seem a viable explanation for the herein observed needle-type structures, which are closely related to large carbide domains. The latter were found for all initial oxide phases, whereas in FH no large carbide domains were developed and, hence, no pronounced needle structures were observed even after 185 h TOS.

Conclusion

Mesoporous iron oxide films with different initial phase and composition were employed to investigate time-dependent phase transformations in the CO_2-FTS at elevated pressure. After 30 h TOS, crystallite growth dominates and reduced iron oxide phases (MAGH/MAGN) result, whereas after 185 h, up to three distinct phases can be observed with varying morphologies (sintered, needle-type, core-shell). The needle-type phase observed in all films, except for FH, was found to represent a low-crystalline iron oxide. Moreover, this phase appears to be formed only after the formation of the sintered MAGH/MAGN and the carbide phase. We assume that oxidation by either CO_2 or H_2O (*via* RWGS) might promote the formation of the needle-type phase. Depending on the initial iron oxide phase, the C=O/C–O contributions increase with a decrease in average oxidation state, hence indicating a higher surface coverage with hydrocarbon species. Based on our previous work, we assume that the carbide phase is formed due to the presence of small amounts of CO formed by the RWGS. A more complex mechanism in CO_2-FTS is evidenced and, beyond that, phase transformation dynamics turn out to be slower compared to those occurring in syngas atmospheres at similar temperature. The initial iron oxide phase only shows a moderate impact on the emerging phases, yet a strong influence on their relative proportions and dimensions. Future studies need to employ in situ techniques to ensure an exclusion of undesired changes due to air exposure. It would also allow to gain time resolved changes in the phase composition.

Experimental Section

For this work mesoporous iron oxide films with different initial phase composition have been employed. A stabilized mesophase obtained after dip-coating of silicon substrates has been exposed to controlled atmospheres during thermal treatment form HEM, FH, MAGH or MAGH/MAGN.

2–Methoxyethanol (99.3 + %, ACS grade) was obtained from Alfa Aesar (Alfa Aesar, Haverhill, USA, Massachusetts), iron nitrate

nonahydrate from (99+%) purchased from Acros Organics (Acros Organics, Fair Lawn, USA, New Jersey), ethanol (99.9+%, ACS grade) was obtained from VWR (Radnor, USA, Pennsylvania). Polymer Service GmbH Merseburg (Polymer Service GmbH, Germany, Merseburg)[33] synthesized and provided the soft template, a copolymer (PEO_{104}–*b*–PB_{92}–*b*–PEO_{104}).

Analogue to previous works the stabilized mesophase has been prepared by an adapted approach[16] developed by Brezesinski *et al.*.[34] PEO_{104}–*b*–PB_{92}–*b*–PEO_{104} (109 mg) was dissolved in a mixture of ethanol (4.36 mL) and 2–methoxyethanol (4.64 mL) for 20 min at 40 °C yielding a colorless solution. Addition of $Fe(NO_3)_3 \cdot 9H_2O$ (1173 mg) and stirring for 1 h at room temperature yielded an orange-red solution which was dip-coated onto Si(100)-wafers.

Mesophase deposition and thermal treatment to form the desired phase composition were carried out analogue to previous works.[16–19] Substrates were dip-coated with a withdrawal rate of 400 mm/min in an argon atmosphere to ensure a low humidity. After drying in argon atmospheres for 10 min, the films were transferred under inert conditions into an oven and calcined in air at 250 h for 1 h. The formed mesophase can be further calcined at 400 °C for 10 min to form FH or at 550 °C for 10 min to form HEM.[16,18] Treatment of the mesophase in N_2 for 5 h at 350 °C yields MAGH. MAGH samples obtained after a thermal treatment at 400 °C for 2 h in N_2, were partially reduced at 350 °C for 1 h in H_2 (4%)/Ar to form MAGH/MAGN films.

For the CO_2 treatment, 4 mm wide coated substrates with HEM, FH, MAGH or MAGH/MAGN films were placed in individual stainless steel reactors operating in parallel in an in-house developed set-up. The reactors were heated up to 200 °C in N_2 and setting the pressure to 20 bar at flow rate of 4.2 mL/min. After a tightness check all reactor have been heated to 300 °C with 5 K/min. Atmosphere was changed to $H_2/CO_2/N_2 = 3:1:0.3$, 20 bar flowrate 3.8 mL/min and treatment has been carried out for 30 h or 185 h respectively. Afterwards, atmosphere was changed to pure N_2 flow at 300 °C and 20 bar. During the following cooldown process (1 K/min) the reactor was depressurized to 1 bar. At the reactor was flushed for 2 h in N_2 to ensure a pressure of 1 bar.

Before TEM analysis, film material was scraped off and placed between two copper grids coated with a carbon film. This allows to protect the microscope from magnetic material escaping the sample holder. The Tecnai G 2 20 S–TWIN (FEI, Hilsboro, USA, Oregon) instrument was operated at 200 kV. SAED pattern were recorded with an aperture with aperture for the investigation of areas with a diameter of 180 nm.

SEM images were recorded using a JEOL 7401F (JEOL, Tokyo, Japan) instrument operated at an acceleration voltage of 10 kV. The working distance was approximately 4.5 mm. Images were analyzed by employing ImageJ (National Institutes of Health, USA, Bethesda).[35]

Grazing incident XRD was performed with a Bruker D8 Advance instrument (Cu Kα radiation, $\lambda = 1.5409$ Å) at an angle of 1 ° for the incident beam. PDFMaintEX library version 9.0.133 (Bruker, Billerica, Massachusetts, USA) was used to assign the recorded reflections. Crystallite sizes were determined for the strongest reflection using the Debye Scherrer equation.

Thermo Fisher Scientific ESCALAB 250Xi (Thermo Fischer Scientific, Waltham, USA, Massachusetts) was used to record XPS spectra with spot sizes of 400 nm and analyzed with the Avantage software. Shirley background with additional constraints was applied to ensure that the intensity of the recorded data is higher than the background for the whole spectrum. Samples were measured without any further preparation on the silicon substrate, however, Si signals were below 2% in intensity.

Scanning transmission electron microscopy (STEM) measurements were performed at 200 kV with a probe aberration-corrected JEM-ARM200F (microscope: JEOL, Japan; corrector: CEOS, Germany) using annular bright field (ABF), annular dark field (ADF) and high angle annular dark field (HAADF) detectors. The microscope is equipped with a DRY-60GV (JEOL) energy-dispersive x-ray-spectrometer (EDXS) and an Enfinium ER electron energy loss spectrometer (EELS, Gatan, USA) for chemical analysis. The sample was deposed on a holey carbon supported Cu-grid (mesh 300) by scraping the catalyst layer off the wafer with a scalpel and without any further pretreatment and transferred to the microscope. Elemental maps of the different elements were calculated from a spectrum image dataset. Differentiation of amorphous and carbidic carbon and carbidic and oxidic iron was achieved by using the electron energy loss fine structure of these elements at different positions as models for a multiple linear least square fit implemented in Gatan Digital Micrograph 3.4.

Acknowledgements

Aleks Arinchtein and Ralph Kraehnert greatly acknowledge the generous fund of the SPP2080 under the DFG-Project 406695057. Marvin Frisch and Meng-Yang Ye appreciate financial support via BMBF ATO-KAT (03EK3052A). Qingxin Yang and Evgenii V. Kondratenko greatly acknowledge the financial support from the Deutsche Forschungsgemeinschaft (DFG) within the priority program SPP 2080 (grant no. KO 2261/10-1). The authors thank ZELMI (TU Berlin) for access to TEM analysis. Funding of EELS from the federal ministry for education and research within the project ESMAC is gratefully acknowledged. Open Access funding enabled and organized by Projekt DEAL.

Conflict of Interest

The authors declare no conflict of interest.

Data Availability Statement

The data that support the findings of this study are available from the corresponding author upon reasonable request.

Keywords: CO_2-FTS · iron catalysts · dynamic changes · mesoporous materials · Auger · XPS · STEM-EELS

[1] B. Yao, T. Xiao, O. A. Makgae, X. Jie, S. Gonzalez-Cortes, S. Guan, A. I. Kirkland, J. R. Dilworth, H. A. Al-Megren, S. M. Alshihri, et al., *Nat. Commun.* **2020**, *11*, 6395.
[2] U. Rodemerck, M. Holeňa, E. Wagner, Q. Smejkal, A. Barkschat, M. Baerns, *ChemCatChem* **2013**, *5*, 1948–1955.
[3] I. Hannula, N. Kaisalo, P. Simell, *C—Journal Carbon Res.* **2020**, *6*, 55.
[4] S. Geng, F. Jiang, Y. Xu, X. Liu, *ChemCatChem* **2016**, *8*, 1303–1307.
[5] W. Wang, S. Wang, X. Ma, J. Gong, *Chem. Soc. Rev.* **2011**, *40*, 3703.
[6] B. Liu, W. Li, J. Zheng, Q. Lin, X. Zhang, J. Zhang, F. Jiang, Y. Xu, X. Liu, *Catal. Sci. Technol.* **2018**, *8*, 5288–5301.

[7] A. S. Skrypnik, Q. Yang, A. A. Matvienko, V. Y. Bychkov, Y. P. Tulenin, H. Lund, S. A. Petrov, R. Kraehnert, A. Arinchtein, J. Weiss, et al., *Appl. Catal. B* **2021**, *291*, 120121.
[8] F. J. Pérez-Alonso, M. L. Granados, M. Ojeda, T. Herranz, S. Rojas, P. Terreros, J. L. G. Fierro, M. Gracia, J. R. Gancedo, *J. Phys. Chem. B* **2006**, *110*, 23870–23880.
[9] Y. Jin, A. K. Datye, *J. Catal.* **2000**, *196*, 8–17.
[10] D. Chakrabarti, A. de Klerk, V. Prasad, M. K. Gnanamani, W. D. Shafer, G. Jacobs, D. E. Sparks, B. H. Davis, *Ind. Eng. Chem. Res.* **2015**, *54*, 1189–1196.
[11] E. De Smit, B. M. Weckhuysen, *Chem. Soc. Rev.* **2008**, *37*, 2758–2781.
[12] R. P. Mogorosi, N. Fischer, M. Claeys, E. van Steen, *J. Catal.* **2012**, *289*, 140–150.
[13] H. M. Torres Galvis, A. C. J. Koeken, J. H. Bitter, T. Davidian, M. Ruitenbeek, A. I. Dugulan, K. P. de Jong, *J. Catal.* **2013**, *303*, 22–30.
[14] J. Li, L. Wu, S. Zhang, J. Wen, M. Liu, C. Wang, X. Li, *Sustain. Energy Fuels* **2019**, *3*, 219–226.
[15] W. Ma, G. Jacobs, U. M. Graham, B. H. Davis, *Top. Catal.* **2014**, *57*, 561–571.
[16] K. Schulz, R. Schmack, H. W. Klemm, A. Kabelitz, T. Schmidt, F. Emmerling, R. Kraehnert, *Chem. Mater.* **2017**, *29*, 1724–1734.
[17] K. Kraffert, A. Kabelitz, K. Siemensmeyer, R. Schmack, D. Bernsmeier, F. Emmerling, R. Kraehnert, *Adv. Mater. Interfaces* **2018**, *5*, 1700960.
[18] A. Arinchtein, R. Schmack, K. Kraffert, J. Radnik, P. Dietrich, R. Sachse, R. Kraehnert, *ACS Appl. Mater. Interfaces* **2020**, *12*, 38714–38722.
[19] A. Arinchtein, M.-Y. Ye, M. Geske, M. Frisch, R. Kraehnert, *Catalysts* **2021**, *11*, 773.
[20] C. J. Brinker, G. C. Frye, A. J. Hurd, C. S. Ashley, *Thin Solid Films* **1991**, *201*, 97–108.
[21] M. Frisch, J. Laun, J. Marquardt, A. Arinchtein, K. Bauerfeind, D. Bernsmeier, M. Bernicke, T. Bredow, R. Kraehnert, *Phys. Chem. Chem. Phys.* **2021**, *23*, 3219–3224.
[22] Y. Jin, H. Xu, A. K. Datye, *Microsc. Microanal.* **2006**, *12*, 124–134.
[23] A. P. Grosvenor, B. A. Kobe, M. C. Biesinger, N. S. McIntyre, *Surf. Interface Anal.* **2004**, *36*, 1564–1574.
[24] M. C. Biesinger, B. P. Payne, A. P. Grosvenor, L. W. M. Lau, A. R. Gerson, R. S. C. Smart, *Appl. Surf. Sci.* **2011**, *257*, 2717–2730.
[25] A. Shchukarev, D. Korolkov, *Open Chemistry* **2004**, *2*, 347–362.
[26] Y. Zhang, C. Cao, C. Zhang, Z. Zhang, X. Liu, Z. Yang, M. Zhu, B. Meng, J. Xu, Y.-F. Han, *J. Catal.* **2019**, *378*, 51–62.
[27] W. E. S. Unger, T. Wirth, V.-D. Hodoroaba, in *Charact. Nanoparticles*, Elsevier, **2020**, pp. 373–395.
[28] M. Bizjak, A. Zalar, P. Panjan, B. Zorko, B. Praček, *Appl. Surf. Sci.* **2007**, *253*, 3977–3981.
[29] A. Schneider, H. Viefhaus, G. Inden, *Mater. Corros.* **2000**, *51*, 338–343.
[30] F. Bonnet, F. Ropital, P. Lecour, D. Espinat, Y. Huiban, L. Gengembre, Y. Berthier, P. Marcus, *Surf. Interface Anal.* **2002**, *34*, 418–422.
[31] T. Riedel, H. Schulz, G. Schaub, K.-W. Jun, J.-S. Hwang, K.-W. Lee, *Top. Catal.* **2003**, *26*, 41–54.
[32] Y. H. Choi, Y. J. Jang, H. Park, W. Y. Kim, Y. H. Lee, S. H. Choi, J. S. Lee, *Appl. Catal. B* **2017**, *202*, 605–610.
[33] B. Eckhardt, E. Ortel, J. Polte, D. Bernsmeier, O. Görke, P. Strasser, R. Kraehnert, *Adv. Mater.* **2012**, *24*, 3115–3119.
[34] K. Brezesinski, J. Haetge, J. Wang, S. Mascotto, C. Reitz, A. Rein, S. H. Tolbert, J. Perlich, B. Dunn, T. Brezesinski, *Small* **2011**, *7*, 407–414.
[35] C. A. Schneider, W. S. Rasband, K. W. Eliceiri, *Nat. Methods* **2012**, *9*, 671–675.

Manuscript received: February 17, 2022
Revised manuscript received: April 12, 2022
Version of record online: ■■, ■■■

RESEARCH ARTICLE

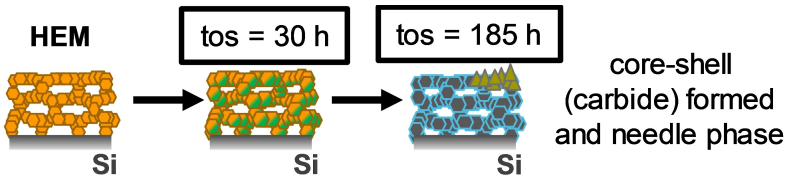

*A. Arinchtein, M.-Y. Ye, Q. Yang, Dr. C. Kreyenschulte, A. Wagner, M. Frisch, Prof. A. Brückner, Prof. E. Kondratenko, Dr. R. Kraehnert**

Dynamics of Reaction-Induced Changes of Model-Type Iron Oxide Phases in the CO_2-Fischer-Tropsch-Synthesis

Dynamic phase transformations of mesoporous iron oxide films in the CO_2-FTS at 300 °C and 20 bar. Carbide structures, resolved by STEM-EELS, evolve after > 30 h TOS and coexist with oxidic phases of different morphologies. This work provides insights into the complex formation mechanism of iron oxides in the CO_2-FTS.